

Article

Effect of Residual Stress on Hydrogen Diffusion in Thick Butt-Welded High-Strength Steel Plates

Jinhui Jiang^{1,2}, Wenshuo Zeng³ and Liangbi Li^{3,*}

¹ State Key Laboratory of Navigation and Safety Technology, Shanghai 200135, China; jiang.jinhui@coscoshipping.com

² Key Laboratory of Marine Technology, Ministry of Communications, Shanghai 200135, China

³ School of Naval Architecture and Ocean Engineering, Jiangsu University of Science and Technology, Zhenjiang 212003, China; zengwenshuo11@163.com

* Correspondence: liliangbi1@126.com

Abstract: Thick high-strength steel plates are increasingly being used for ship structures. Moreover, hydrogen enters the process of manufacturing and service, and large residual tensile stress occurs near the weld. Such stress can facilitate the diffusion and accumulation of hydrogen in the material, leading to hydrogen embrittlement fracture of the shell. Therefore, residual-stress-induced diffusion and accumulation of hydrogen in the stress concentration region of thick butt-welded high-strength steel plate structures need to be studied. In this study, manual metal arc welding was realized by numerical simulation of residual stress in a thick butt-welded high-strength steel plate model using the thermoelastic–plastic theory and a double ellipsoidal heat source model. To analyze residual stress, a set of numerical simulation methods was obtained through comparative analysis of the test results of relevant literature. Residual and hydrostatic stress distributions were determined based on these methods. Then, hydrogen diffusion parameters in each region of the model were obtained through experimental tests. Finally, the results of the residual stress field were used as the predefined field of hydrogen diffusion to conduct a numerical simulation analysis. The distribution of hydrogen diffusion under the influence of residual stress was obtained based on the theory of stress-induced hydrogen diffusion. The weak area of the welding joint was found to be near the weld toe, which exhibited high hydrostatic stress and hydrogen concentration. Further, the maximum hydrogen concentration value of the vertical weld path was approximately 6.1 ppm, and the maximum value of the path parallel to the weld centerline and 31 mm away from the weld centerline was approximately 6.22 ppm. Finally, the hydrostatic tensile stress in the vertical weld path was maximized (~345 MPa), degrading the material properties and causing hydrogen-related cracking. Hence, a reliable method for the analysis of hydrogen diffusion according to residual stress in thick high-strength steel plates was obtained. This work could provide a research basis for controlling and eliminating the adverse effects of hydrogen on the mechanical properties of ship structures and ensuring the safe service of marine equipment.



Citation: Jiang, J.; Zeng, W.; Li, L. Effect of Residual Stress on Hydrogen Diffusion in Thick Butt-Welded High-Strength Steel Plates. *Metals* **2022**, *12*, 1074. <https://doi.org/10.3390/met12071074>

Academic Editor: Paolo Ferro

Received: 21 May 2022

Accepted: 15 June 2022

Published: 23 June 2022

Publisher's Note: MDPI stays neutral with regard to jurisdictional claims in published maps and institutional affiliations.

Keywords: welding residual stress; high-strength steel; thick butt-welded plate; hydrogen diffusion; numerical simulation; manual electric arc welding; manual metal arc welding



Copyright: © 2022 by the authors. Licensee MDPI, Basel, Switzerland. This article is an open access article distributed under the terms and conditions of the Creative Commons Attribution (CC BY) license (<https://creativecommons.org/licenses/by/4.0/>).

1. Introduction

Water will decompose into hydrogen and enter liquid metal during the smelting process of metal materials. Hydrocarbons in fuel may also introduce hydrogen. Although the dehydrogenation process is performed after the metal solidifies into casting embryo, the presence of hydrogen in the metal cannot be completely avoided. Moreover, ship structures are generally large-scale welded structures, whereas welding is actually a local smelting process. The moisture contained in the welding rod and coating easily decomposes into hydrogen atoms and enters the metal. The continuous high pressure borne by an

underwater ship structure during service will promote the destruction of Cl^- on its passive film and the adsorption and penetration of hydrogen (H) on the material surface. As a result, hydrogen evolution reaction occurs easily. Thick high-strength steel plates are widely used in ship structures, but large residual tensile stress occurs near the weld [1,2]. The chemical potential of hydrogen is changed because residual stress interacts with the strain field of hydrogen, thus inducing hydrogen to diffuse and accumulate in the region of stress concentration [3–6].

Hydrogen can reduce the properties of materials and is often accompanied by hydrogen embrittlement (HE) [7,8]. The entry of hydrogen into materials is harmful in general, giving rise to issues such as microcracks caused by hydrogen pressure (or welding cold cracks), hydrogen-induced plastic loss, and hydrogen-assisted cracking (HAC) or fracture. The occurrence of brittle fracture is concealed by the combined action of hydrogen and residual stress. Brittle fracture will occur suddenly once the critical point is reached, often causing personal danger and great economic loss. This paper provides a research basis for controlling and eliminating the adverse effects of hydrogen on the mechanical properties of ships and offshore structures and ensuring the safe service of large offshore equipment.

Roy et al. [9] analyzed the strength and failure mode of screw under corrosion by comparing the finite element calculation and test results. Feng et al. [10] studied the stress concentration factors (SCFs) of stainless steel welded joints. Jacek et al. [11] studied the possibility of underwater wet welding of covered electrode S1300 ultra-high-strength steel of different thicknesses. However, neither work considered the effect of hydrogen.

Thus, Pandey et al. [12] used numerical simulation method to study the relationship between hydrogen diffusion behavior and bending stress of P91 steel under multipass welding. Jiang et al. [13–15] numerically simulated the hydrogen diffusion behavior induced by the welding residual stress of 16MnR steel with a wall thickness of 30 mm in a wet hydrogen sulfide environment. Lv et al. [16] studied the plane geometry model of a quarter section of a titanium alloy cylinder with a diameter of 100 mm \times 60 mm and then conducted a simple numerical analysis of hydrogen diffusion behavior under the action of residual stress at a welded joint. However, the yield strength of the studied material was relatively low. Li et al. [17] conducted a numerical study on the influence of hydrogen on the residual stress of a medium-thickness steel plate with a yield strength of approximately 600 MPa at an early stage. However, these investigations did not consider hydrogen diffusion experimental studies.

Zhang et al. [18–21] studied the buckling strength of the pressure spherical shell formed by the butt-welded method but did not consider the influence welding residual stress and hydrogen diffusion would have on their results. Zhang [22] and Zhang et al. [23–25] studied the hydrogen permeation behavior of welded joints of X80 pipeline steel with a wall thickness of 18.4 mm using a high-pressure gaseous hydrogen permeation test device. Gong [26] and Yan et al. [27–29] measured the parameters related to hydrogen diffusion using the electrochemical penetration method and numerically simulated the variation of hydrogen concentration and residual stress in welded joints of 12 mm thick 16MnR steel and X80 pipeline steel. de Souza Sant'Anna et al. [8] studied the influence of hydrotreatment on residual stress in an API 5L X65 steel pipe with a wall thickness of 9.5 mm using the electrochemical method. Although these studies investigated the influence of welding residual stress on hydrogen diffusion through a combination of numerical simulations and experiments, they focused only on thin shells or thin plates with low yield strength.

Although previous studies have investigated both residual stress and hydrogen diffusion, no study has simultaneously investigated these behaviors in thick high-strength steel plates using numerical simulations informed by laboratory tests, representing the novelty of our study.

The main contribution of this study to the field of manufacturing technology is a reliable method for the analysis of hydrogen diffusion according to residual stress in thick high-strength steel plates, such as those commonly used in the construction of ship hulls. The findings of this study can therefore be used by ship fabricators to improve

industrial applications of welding procedures to reduce residual stresses in key locations and thereby avoid hydrogen-related cracking and deterioration of ship hulls. The results of this study clarify this relationship and can be used to establish a foundation for improved hull fabrication design and welding procedures.

2. Basic Theory and Analysis Method

2.1. Basic Form of Welding Heat Transfer Process

① Heat conduction is expressed by the following equation [30]:

$$q'' = -\lambda \frac{\partial T}{\partial n} \quad (1)$$

where q'' is the heat flux in W/m^2 , λ is the thermal conductivity in $W/(mm \cdot ^\circ C)$, and $\partial T/\partial n$ denotes the temperature gradient in $^\circ C/mm$.

② Convection heat transfer is as follows [30]:

$$q_k = h(T_w - T_f) \quad (2)$$

where h is the heat transfer coefficient, and T_w , T_f are the surface temperatures of the fluid and the solid, respectively.

③ Radiation heat transfer is expressed as follows [30]:

$$q = \varepsilon C_0 A_1 F_{12} (T_1^4 - T_2^4) \quad (3)$$

where q denotes the heat flow rate, and ε is the object's blackness coefficient or emissivity. C_0 represents the radiation coefficient of the absolute black body and can be calculated as $C_0 = 5.67 \times 10^{-14}$ ($W/(mm^2 \cdot ^\circ C)$). This is applicable to the object that can completely absorb the radiant energy falling on it, or "absolute black body", where $\varepsilon = 1$, A_1 is the area of radiant surface 1, F_{12} is the shape coefficient from radiant surface 1 to radiant surface 2, T_1 denotes the absolute temperature of radiant surface 1, and T_2 denotes the absolute temperature of radiant surface 2.

2.2. Basic Theory of Thermoelastoplasticity

2.2.1. Stress–Strain Relationship

The stress–strain relationship of the material in elastic or plastic state is as follows [31]:

$$\{d\sigma\} = [D]\{d\varepsilon\} - \{C\}dT \quad (4)$$

where $[D]$ is the elastic or elastoplastic matrix, and $\{C\}$ is the vector related to temperature.

In the elastic zone, let the yield condition of the material be as follows [31]:

$$\{D\} = \{D\}_e \quad (5)$$

$$\{C\} = \{C\}_e = [D]_e \left(\{a\} + \frac{\partial [D]_e^{-1}}{\partial T} \{\sigma\} \right) \quad (6)$$

where a is the coefficient of linear expansion, and T is the temperature.

In the plastic zone, it is assumed that the yield condition of the material is as follows [31]:

$$f(\sigma) = f_0(\varepsilon_p, T) \quad (7)$$

where f is the yield function, and f_0 is the function of yield stress. The plastic strain increment $d\varepsilon_p$ according to the plastic flow law can be expressed as follows [31]:

$$d\varepsilon_p = \lambda \frac{\partial f}{\partial \sigma} \quad (8)$$

The unloading of the plastic zone is judged by the value of λ , and the unloading process corresponds to negative λ values.

2.2.2. Equilibrium Equation

A certain element of the structure has the following balance equation [31]:

$$\{dF\}^e + \{dR\}^e = [K]^e \{d\delta\}^e \quad (9)$$

where $\{dF\}^e$ is the increment of the nodal force of the element, $\{dR\}^e$ is the increment of equivalent node of element initial stress change caused by temperature, $\{d\delta\}^e$ is the node displacement increment, and $[K]^e$ is the element stiffness matrix.

After integrating the total stiffness matrix $[K]$ and the total load vector $\{dF\}$, the balance equations of the whole welded member are as follows [31]:

$$[K]\{d\delta\} = \{dF\} \quad (10)$$

where $[K] = \sum [K]^e$, $\{dF\} = \sum (\{dF\}^e + \{dR\}^e)$.

2.2.3. Equation Solution

The welding stress field is solved using the finite element method of thermoelastic–plastic stress analysis. The main process is as follows. First, the welding structure is divided using the finite element method. Then, based on the calculation of welding temperature field, a temperature increment is gradually applied. Finally, the displacement increment of each node can be calculated according to Equation (4). The relationship between the strain increment and the node displacement increment in each element is as follows [31]:

$$d\epsilon^e = Bd\delta^e \quad (11)$$

Then, the stress increment can be obtained from the stress–strain relationship $d\sigma = Dd\epsilon - CdT$; thus, the welding stress field can be obtained.

2.3. Hydrogen Diffusion

The diffusion phase should satisfy the law of mass conservation during diffusion as follows [32]:

$$\int_V \frac{dC}{dt} dV + \int_S n \cdot J dS = 0 \quad (12)$$

where V denotes the arbitrary volume of surface S , C is the diffusion phase concentration, t denotes time, n is the outward normal direction of S , J is the concentration flow of the diffusion phase, and $n \cdot J$ represents the concentration flow exiting surface S .

Diffusion is driven by the general chemical potential gradient; thus, the diffusion behavior can be expressed as follows [16]:

$$J = -sD \cdot \left(\frac{\partial \phi}{\partial x} + K_s \frac{\partial}{\partial x} (\ln(\theta - \theta_z)) + K_p \frac{\partial p}{\partial x} \right) \quad (13)$$

$$c = \phi s \quad (14)$$

where D is the diffusion coefficient of hydrogen; K_s is the “Soret effect” coefficient driven by the temperature gradient; θ denotes the temperature; θ_z is the absolute zero temperature on the temperature scale used; K_p is the stress coefficient driven by the stress gradient; $p = -\text{trace}(\sigma)/3$ represents the equivalent stress, wherein σ denotes stress; c is the concentration of hydrogen; ϕ is the normalized concentration of the diffused phase, also known as the activity of the diffused material; and s is the solubility of the diffused material in the substrate.

If D , K_s , or K_p depend on the hydrogen concentration, the problem becomes nonlinear and equations become asymmetric. In practical engineering applications, the dependence on hydrogen concentration is strong. Therefore, the asymmetric matrix storage and solution scheme is automatically invoked when mass diffusion analysis is carried out.

The mass diffusion behavior is usually described by Fick's law as follows [16]:

$$J = -D \left(\frac{\partial c}{\partial x} + sK_p \frac{\partial p}{\partial x} \right) \quad (15)$$

$$K_p = \phi \frac{\bar{V}_H}{R(\theta - \theta_z)} \quad (16)$$

2.4. Analytical Methods

Here, we used the basic theory of thermoelastoplasticity to numerically simulate the residual stress field of a thick butt-welded high-strength steel plate (hereafter known as Model I) and compared the simulation results with test results in the literature. Based on the agreement between numerical simulation and test results from the literature, a verified residual stress analysis method for a thick butt-welded high-strength steel plate was obtained. This method was then applied to the numerical simulation of the residual stress in a thick butt-welded high-strength steel plate (hereafter referred to as Model II). Simultaneously, the parameters related to hydrogen diffusion in Model II were experimentally studied, and the hydrogen diffusion coefficient and content were obtained and applied in the residual stress analysis of Model II. Based on the basic theory of residual-stress-induced hydrogen diffusion, hydrogen diffusion was numerically simulated in Model II under the influence of residual stress. Finally, a set of analytical methods for hydrogen diffusion induced by welding residual stress was obtained, as shown in Figure 1. These methods represent a new analysis method for studying the diffusion of hydrogen according to welding residual stress in thick butt-welded high-strength steel plates.

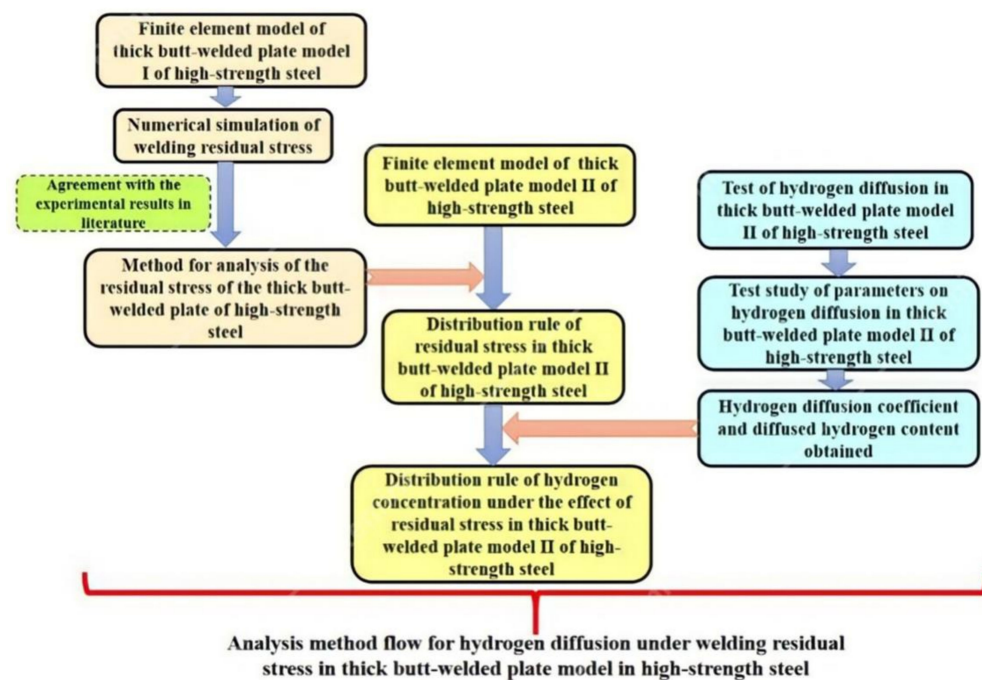


Figure 1. Method flow diagram for hydrogen diffusion analysis.

3. Numerical Simulation

A thick butt-welded high-strength steel plate was analyzed in this study according to the basic theory of thermoelastoplasticity and the given temperature method [33,34]. The finite element software ABAQUS (6.1., Dassault Systèmes, Johnston, RI, USA) was used to simulate the distribution of welding residual stress, which was then compared with the relevant test results from the study of Sun [35]. The numerical simulation results for residual stress were thus verified, providing a theoretical basis for subsequent research on the effect of residual stress on the hydrogen diffusion of thick butt-welded high-strength steel plates.

3.1. Numerical Simulation and Experimental Verification of Residual Stress in Model I

3.1.1. Finite Element Model and Material Properties of Model I

The plate for Model I consisted of two thick high-strength steel plates with dimension of 250 mm × 125 mm × 38 mm and yield strength of 918 MPa, joined by an x-groove butt weld. The weld width on the surface of the plate was 22 mm, as shown in Figure 2.

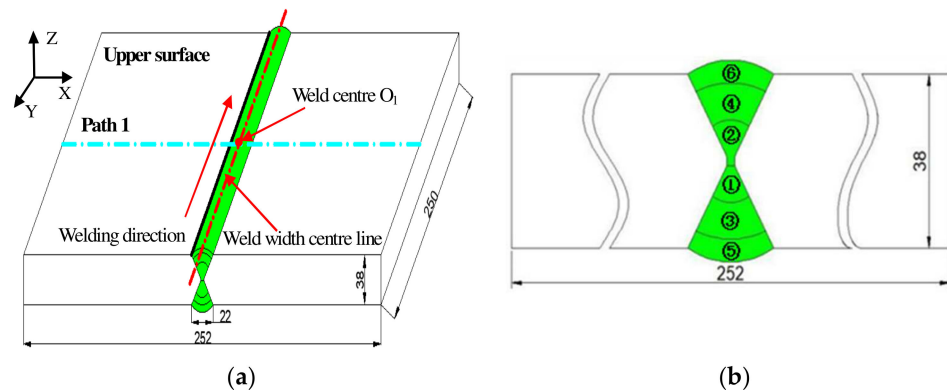


Figure 2. Model I (in mm): (a) geometric dimensions and weld path; (b) welding sequence (①–⑥).

Table 1 and Figure 3 show the thermophysical properties and mechanical parameters of the material in Model I at different temperatures.

Table 1. Thermophysical properties of materials in Model I [35].

Temperature (°C)	Elastic Modulus (MPa)	Poisson's Ratio	Thermal Expansion Coefficient (1/°C)	Heat Transfer Coefficient (W/(m·°C))	Specific Heat (J/(kg·°C))
25	1.96×10^5	0.3	1.2×10^{-5}	16.3	450
500	1.4275×10^5	0.3	1.58×10^{-5}	16.3	707
1000	0.7575×10^5	0.3	1.72×10^{-5}	16.3	1730
1300	0.0425×10^5	0.3	1.86×10^{-5}	16.3	6800

The welding method used was manual electric arc welding. Model I was joined by the positive and negative alternating multilayer and multipass welding method. To improve calculation efficiency and ensure calculation accuracy, the numerical simulation was simplified into six layers along the direction of the weld thickness according to the welding sequence shown in Figure 2b. The finite element model of Model I was created with the mesh shown in Figure 4, in which the uneven grid division method was applied. For the welding seam and heat-affected zone, a refined Hex-grid with a grid size of 2 mm × 2 mm × 4 mm was adopted to improve calculation accuracy. The mesh size gradually increased from the weld to the base metal area, and the maximum mesh size was 4 mm × 8 mm × 15 mm. There were 38,173 nodes and 34,568 elements in Model I.

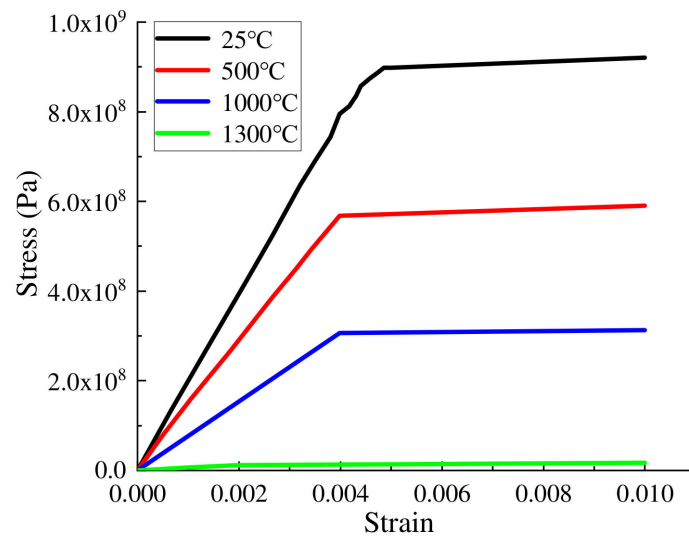


Figure 3. Stress–strain curves of the material in Model I according to temperature.

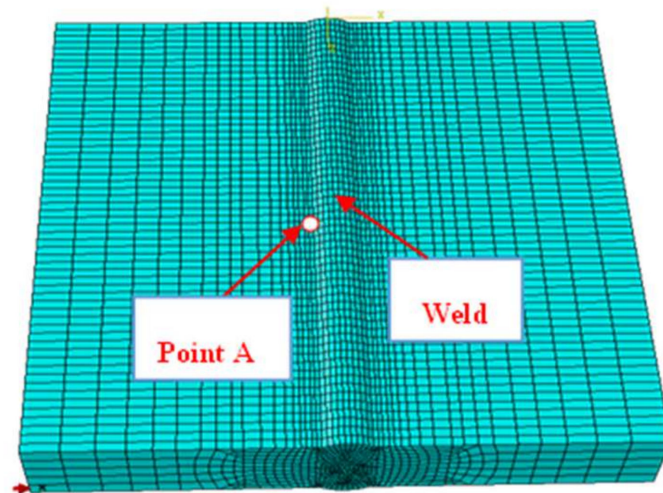


Figure 4. Finite element model and mesh division of Model I.

3.1.2. Numerical Simulation of Welding Residual Stress in Model I

To effectively simulate the welding process, the DFLUX subroutine and double ellipsoidal heat source model [36] in ABAQUS were applied in this study. The latter is illustrated in Figure 5, where a is half the width of the heat source, b is the depth of the heat source, c_f represents the front-half of the heat source, and c_r represents the rear-half of the heat source. The actual welding process was simulated using the “birth and death element” method. The heat input was controlled by the parameters of the double ellipsoidal heat source model and the applied current and voltage to calculate and analyze the temperature field. During numerical simulation of the welding residual stress, the four corners of Model I were rigidly fixed to simulate the constraint conditions of the actual welding process. The welding thermal efficiency was 0.85, the ambient temperature was set at 25 °C, and the convection heat transfer coefficient was 62.5 W/m²·°C. The shape parameters of the double ellipsoidal heat source model were adjusted to ensure that the simulation results of the temperature field were close to the results of the actual welding process. The final shape parameters are shown in Table 2.

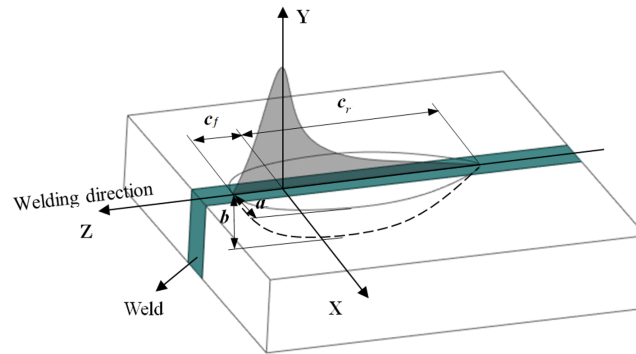


Figure 5. Double ellipsoidal heat source model.

Table 2. Double ellipsoid heat source shape parameters of Model I.

Half Width of Heat Source a_1 (m)	Depth of Heat Source b_1 (m)	Front Half of Heat Source C_{f1} (m)	Back Half of Heat Source C_{r1} (m)	Energy Fraction of the Anterior Portion of the Ellipsoid	Energy Fraction of the Latter Part of the Ellipsoid
0.025	0.015	0.025	0.1	0.6	1.4

Point A was selected near the weld on the upper surface (Figure 2a) of Model I, and the change in temperature at point A over time is shown in Figure 6. Before the maximum temperature of 1300 °C was reached, there was a local maximum (Figure 6) caused by the heat source passing close to point A when welding the previous (fourth) weld layer on the same side of the sixth layer (Figure 2b). Then, the heat source was moved to the opposite side of the fifth weld layer, and the temperature of point A decreased. Subsequently, the temperature increased to the maximum value and finally decreased to room temperature to stabilize.

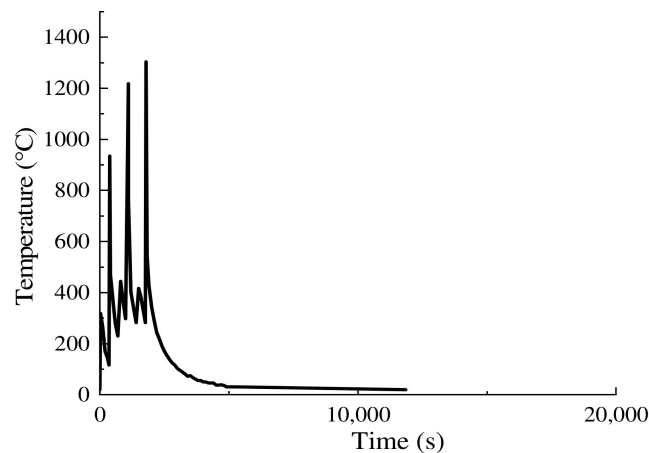


Figure 6. Temperature change curve at Point A in Model I.

As shown in Figure 2a, the centerline of the weld width on the upper surface of Model I was oriented along the Y-axis, and the center point O_1 was set as the origin of the coordinate system. The X-axis was oriented perpendicular to the weld, passing through the weld center O_1 , and the Z-axis was oriented perpendicular to the upper surface of the plate. Finally, Path 1 in Figure 2a was defined along the X-axis. The residual stress on the upper surface perpendicular to the direction of the weld is referred to as the transverse residual stress, and the residual stress along the weld direction is referred to as the longitudinal residual stress. Note that these definitions of residual stress are applicable to the butt-welded Model II discussed in Section 3.2.

The transverse residual stress σ_{x1} and longitudinal residual stress σ_{y1} in Model I when steady state was reached are shown in Figure 7 and compared with the test results from the study of Sun [35] along Path 1 in Figure 8.

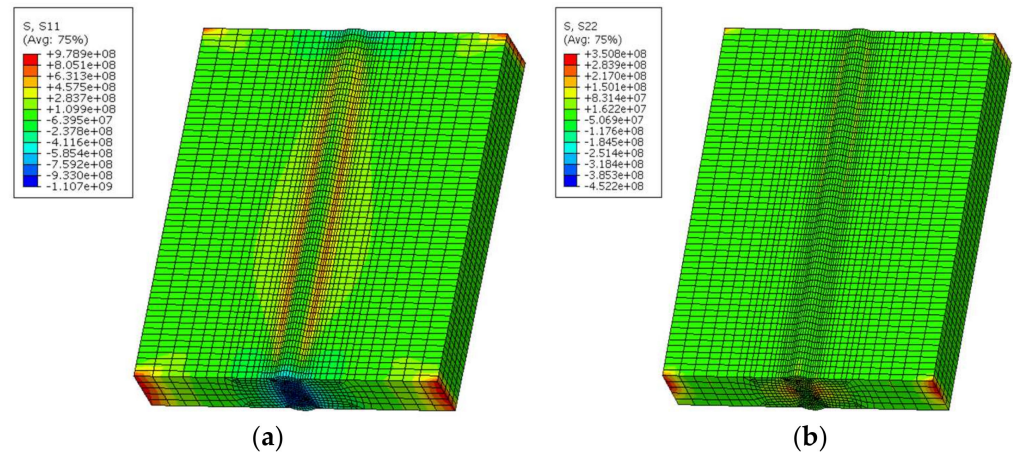


Figure 7. Residual stress distribution in Model I: (a) transverse residual stress; (b) longitudinal residual stress.

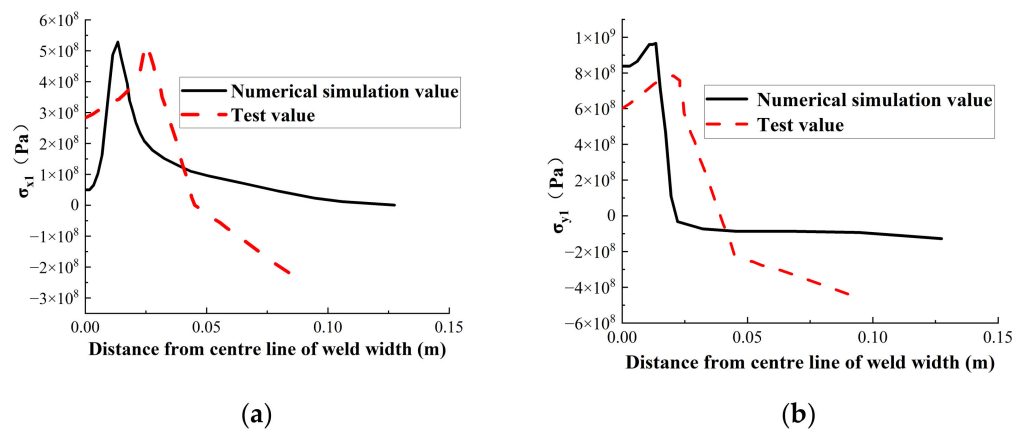


Figure 8. Numerical simulation results of residual stress along Path 1 and test results from [35] for (a) transverse residual stress σ_{x1} ; (b) longitudinal residual stress σ_{y1} .

As shown in Figures 7 and 8, the transverse residual stress σ_{x1} and longitudinal residual stress σ_{y1} along Path 1 of Model I exhibited bimodal distributions, and the residual stresses, which were tensile, were the largest near the weld. Furthermore, the longitudinal residual stress was found to be greater than the transverse residual stress. The maximum values of the transverse and longitudinal residual stresses were approximately 520 and 950 MPa, respectively. As the distance from the weld increased, the residual stress decreased gradually. Moreover, the numerical simulation results of the transverse and longitudinal residual stresses were consistent with the test results of Sun [35].

Therefore, the numerical simulation method used to model the residual stress of a thick butt-welded high-strength steel plate was considered feasible, establishing the foundation for the influence of residual stress on hydrogen diffusion.

3.2. Numerical Simulation of Residual Stress in Model II

3.2.1. Finite Element Model and Material Properties of Model II

Model II consisted of two pieces of Marine 10Ni5CrMoV steel [37] having the dimension of 500 mm \times 200 mm \times 40 mm with the yield strength of 785 MPa, which is relatively tough and strong. A V840 electrode with a diameter of 4 mm was used, and the groove

chamfer was 10°. The weld width of the upper surface was 44 mm. The geometry of Model II is shown in Figure 9a.

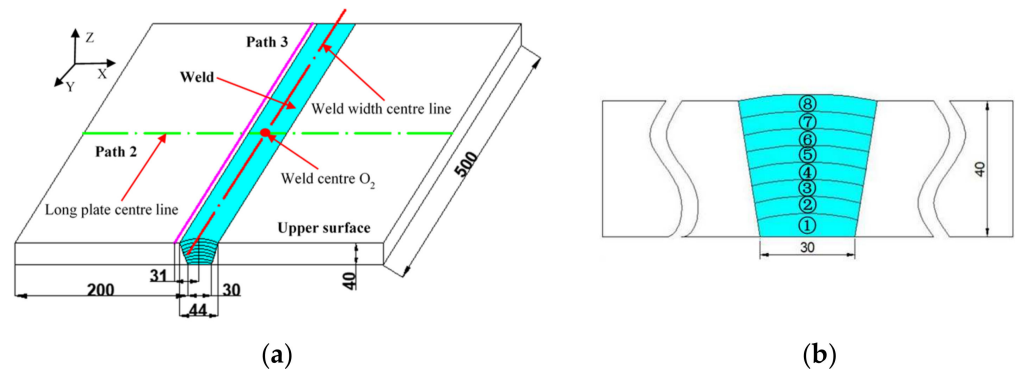


Figure 9. Model II (in mm): (a) geometric dimensions and weld path; (b) welding sequence (①–⑧).

The numerical simulation was simplified to eight layers along the direction of the weld thickness to improve calculation efficiency, as shown in the welding sequence in Figure 9b. A finite element model was created as shown in Figure 10. During the mesh division of Model II, the mesh near the weld was denser with a refined Hex-grid and a size of 2.5 mm × 2.5 mm × 5 mm, whereas the mesh density farther from the weld was sparse and the maximum mesh size was 5 mm × 7 mm × 25 mm. There were 100,697 nodes and 92,800 elements in Model II.

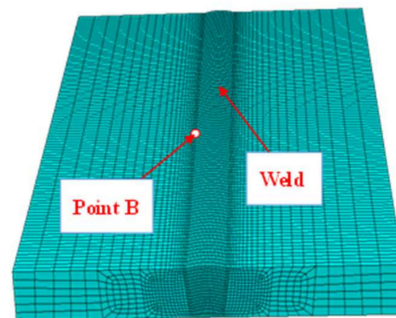


Figure 10. Finite element model and mesh division of Model II.

The material parameters [38] of Model II at different temperatures are shown in Figure 11, and the physical property parameters at other temperatures were obtained using the linear interpolation method. It was assumed that the weld and base metal were of the same material with the same physical properties.

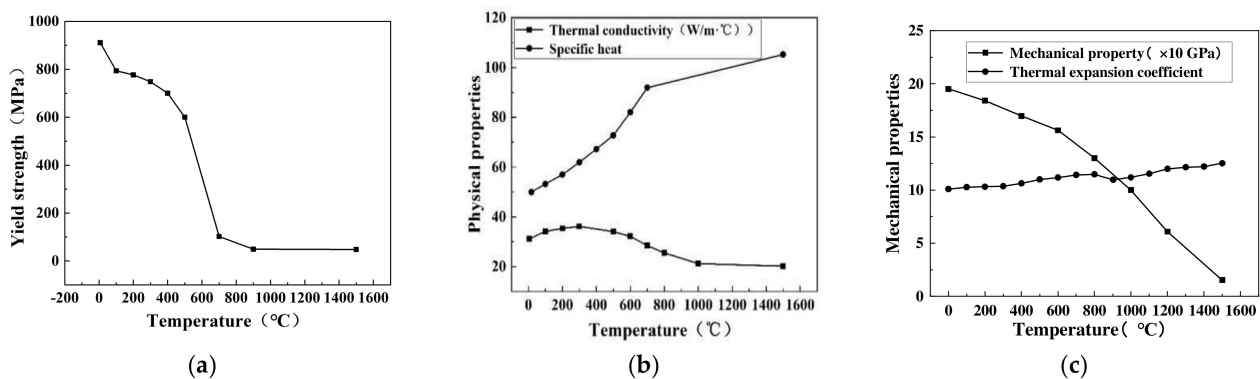


Figure 11. Material parameters of Model II: (a) strength parameters; (b) physical performance parameters; (c) mechanical parameters.

3.2.2. Numerical Simulation of Welding Residual Stress in Model II

The highest temperature at the weld was ~ 1500 °C [38], and the welding thermal efficiency was 0.85. In the analysis of the temperature field, the ambient temperature and initial temperature were both set to 25 °C, and the convective heat transfer coefficient was set to $40 \text{ W/m}^2 \cdot \text{°C}$ [38]. After repeated debugging, the shape parameters of the double ellipsoidal heat source model were obtained (Table 3).

Table 3. Double ellipsoid heat source shape parameters of Model II.

Half Width of the Heat Source a_2 (m)	Depth of the Heat Source b_2 (m)	Front Half of the Heat Source C_{f2} (m)	Back Half of the Heat Source C_{r2} (m)	Energy Fraction of the Anterior Portion of the Ellipsoid	Energy Fraction of the Latter Part of the Ellipsoid
0.025	0.007	0.025	0.1	0.8	1.2

The welding temperature field and welding residual stress field of Model II were obtained using the same method used for calculating the residual stress field of Model I. Point B was selected near the weld on the upper surface of Model II (Figure 10), and its temperature change over time is shown in Figure 12. The maximum temperature at Point B was approximately 1500 °C. Before reaching this maximum temperature, seven local maxima were observed, the values of which increased sequentially and finally decreased to room temperature to reach a stable state. The temperature increased at Point B as a result of the preheating effect of the welding heat source.

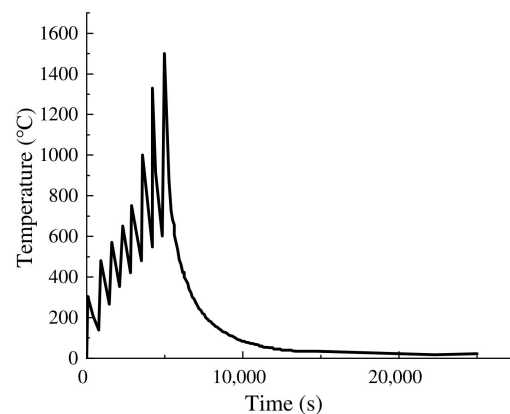


Figure 12. Temperature change curve at Point B in Model II.

As shown in Figure 9a, the centerline of the weld width on the upper surface of Model II was oriented along the Y-axis and the midpoint O_2 was chosen as the origin for the coordinate system, from which the X-axis was defined and passed through the weld center O_2 and the Z-axis was oriented perpendicular to the upper surface and passed through the weld center O_2 . The centerline of the plate length located on the upper surface of the final weld layer (layer 8) along the X-direction was defined as Path 2, and Path 3 extended along the weld toe, parallel to and 31 mm away from the centerline of the weld.

Hydrogen diffusion is affected by the hydrostatic stress $\sigma_h = (\sigma_x + \sigma_y + \sigma_z)/3$, where σ_x is the transverse residual stress, σ_y is the longitudinal residual stress, and σ_z is the vertical residual stress. The equivalent compressive stress $\sigma_{pressure}$ is the negative value of the hydrostatic stress σ_h affecting hydrogen diffusion [23], expressed as $\sigma_{pressure} = -(\sigma_x + \sigma_y + \sigma_z)/3$. Figure 13 shows the transverse residual stress σ_{x2} , longitudinal residual stress σ_{y2} , equivalent compressive stress $\sigma_{pressure}$, and von Mises stress of Model II after numerical simulation analysis when steady state was reached.

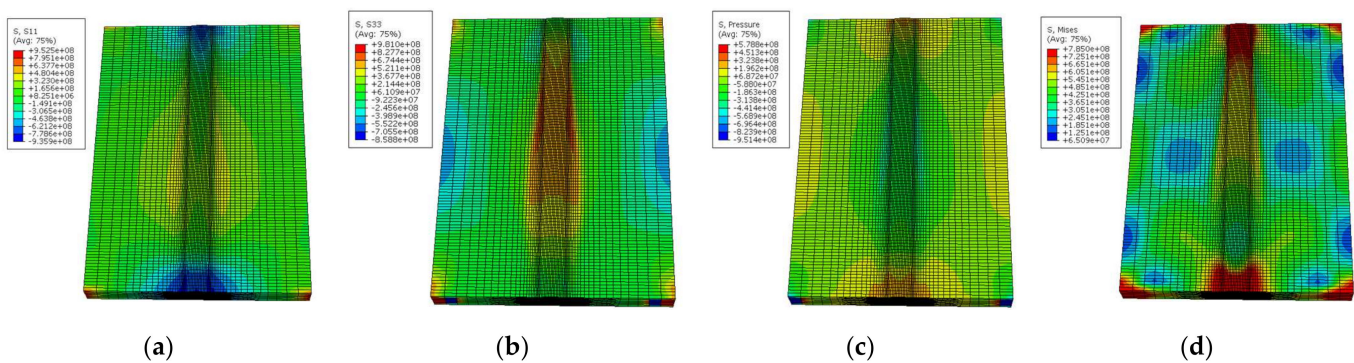


Figure 13. Residual stress in Model II: (a) transverse residual stress σ_{x2} ; (b) longitudinal residual stress σ_{y2} ; (c) equivalent compressive stress $\sigma_{pressure}$; (d) von Mises stress.

The distribution of hydrostatic stress affecting hydrogen diffusion along Paths 2 and 3 is shown in Figure 14, in which σ_h is shown to exhibit a symmetrical bimodal distribution along Path 2 with a maximum value of ~ 345 MPa located near the weld toe that gradually decreased with the increase in distance from the weld. Along Path 3, σ_h is shown as the tensile stress, and the value of the maximum stress was approximately 334 MPa.

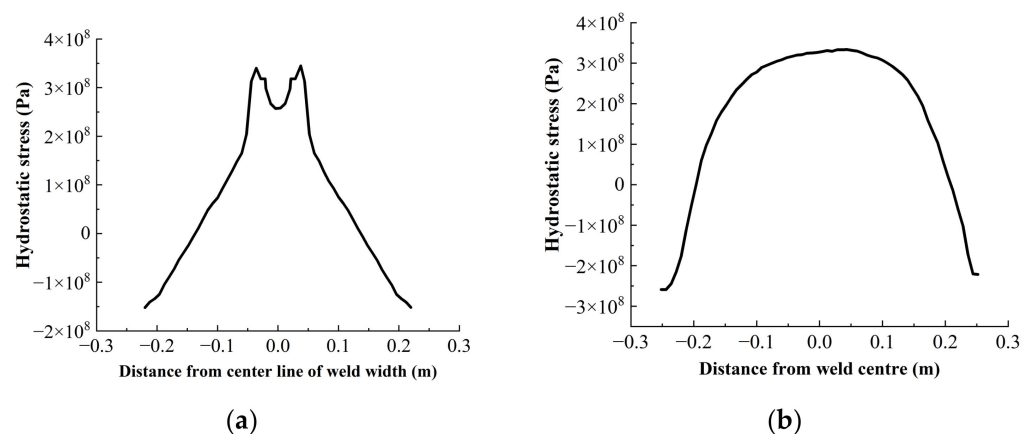


Figure 14. Hydrostatic stress distribution of Model II for (a) Path 2; (b) Path 3.

4. Hydrogen Diffusion under the Effect of Residual Stress in Model II

The relevant parameters of hydrogen diffusion in Model II were studied experimentally. Then, based on the results of the hydrogen diffusion coefficient and the diffused hydrogen content obtained from the test, the hydrogen diffusion of Model II under the influence of residual stress was numerically simulated using the basic theory of hydrogen diffusion induced by residual stress.

4.1. Experimental Study of Diffusion Coefficient and Diffused Hydrogen Content of Model II

The hydrogen diffusion coefficient in Model II (Figure 9) under different tensile stresses in the weld zone was determined using the electrochemical hydrogen penetration method in both the heat-affected zone and base-metal zone. This is because the hydrogen diffusion coefficient depends on the region owing to the heterogeneity of the welded joint. The diffused hydrogen content of the deposited metal from the sample welding rod was measured using the thermal conductivity method (hydrogen collection method), which provided the relevant parameters for studying the influence of welding residual stress on the hydrogen diffusion of Model II.

4.1.1. Measurement of Hydrogen Diffusion Coefficient in Different Regions of Model II

The hydrogen diffusion coefficient was measured using a CS2350 two-unit electrochemical workstation (Figure 15a). Samples with a thickness of 1 mm were collected from the weld, heat-affected zone, and base metal of Model II by wire cutting after welding. The sampling locations are shown in Figure 15b, and the completed samples are shown in Figure 15c.

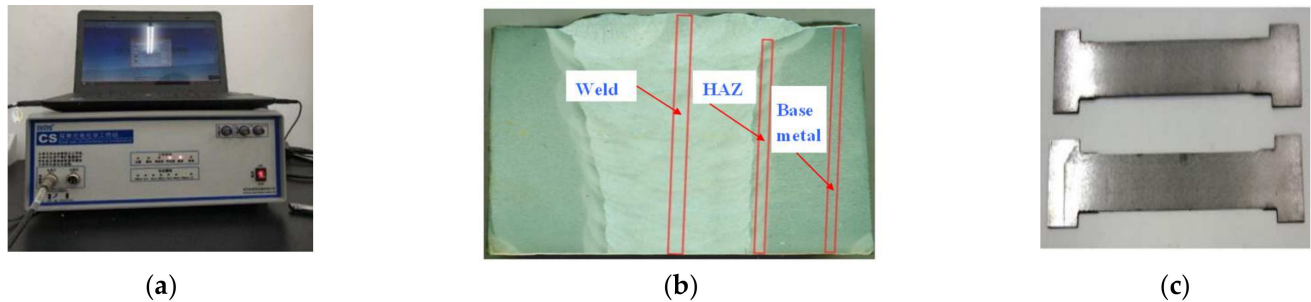


Figure 15. Specimen preparation: (a) CS2350 two-unit electrochemical workstation; (b) sampling locations on Model II; (c) finished samples.

To prevent hydrogen diffusion from one side of the specimen to the other, each specimen was plated with nickel on one side. The nickel plating process is shown in Figure 16a. A double electrolytic cell device was used in the hydrogen permeation test (Figure 16b). The device consisted of two distinct electrolytic cells. Figure 16c shows the device to which tension was applied.

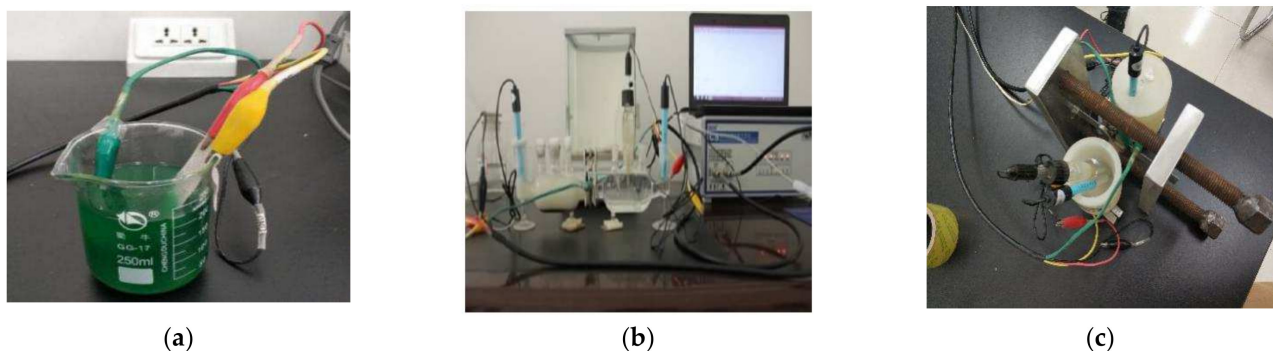


Figure 16. Test device: (a) nickel plating device for sample; (b) schematic of hydrogen permeation test device; (c) device for tension application.

In the electrochemical hydrogen permeation test, hydrogen extraction treatment was carried out on each sample to extract residual hydrogen so that it would not influence the test results. Then, the sample was charged with hydrogen and its hydrogen permeation curve was obtained, as shown in Figure 17. The maximum current measured in the anode chamber was designated as I_{max} , and the current I_t at $I_t/I_{max} = 0.63$ [39] and its corresponding lag time t_L were obtained. The hydrogen diffusion coefficient D and electrolytic hydrogen charging concentration C in each region of Model II were calculated as follows [40–42]:

$$D = \frac{L^2}{6t_L} \quad (17)$$

$$C = \frac{I_{max}L}{2FD} \quad (18)$$

where L denotes the thickness of the sample, and F is the Faraday constant [43].

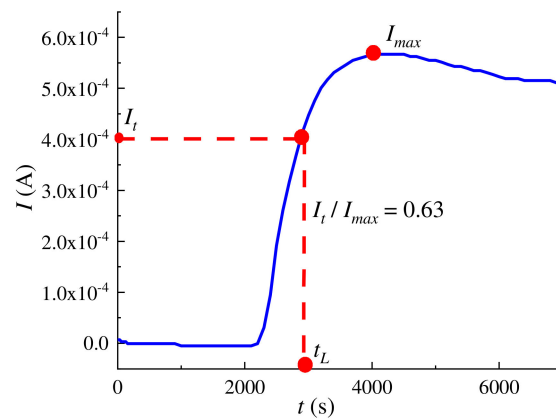


Figure 17. Hydrogen permeation curve.

The lag times t_L corresponding to $I_t/I_{max} = 0.63$ obtained for the weld, heat-affected zone, and base metal of Model II under different tensile stresses are shown in Figure 18. The hydrogen diffusion coefficient D and electrolytic hydrogen charging concentration C of Model II in different regions according to Equations (17) and (18) are shown in Table 4.

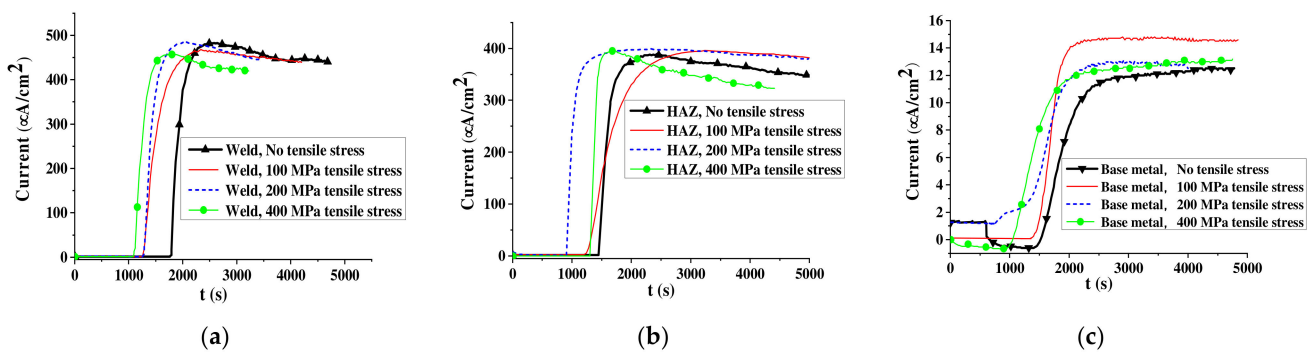


Figure 18. Hydrogen permeation curves for Model II under different tensile stresses in the (a) weld; (b) heat-affected zone (HAZ); (c) base metal.

Table 4. Hydrogen diffusion coefficient D and electrolysis hydrogen charging concentration C of each region of Model II under different tensile stresses.

Tensile Stress MPa	Weld		Heat-Affected Zone		Base Metal	
	D_1 $\times 10^{-7} \text{ cm}^2/\text{s}$	C_1 $\times 10^{-4} \text{ mol}/\text{cm}^3$	D_2 $\times 10^{-7} \text{ cm}^2/\text{s}$	C_2 $\times 10^{-4} \text{ mol}/\text{cm}^3$	D_3 $\times 10^{-7} \text{ cm}^2/\text{s}$	C_3 $\times 10^{-4} \text{ mol}/\text{cm}^3$
0	4.48	4.032	4.55	3.058	4.16	0.110
100	5.67	3.076	4.90	2.803	4.33	0.123
200	6.04	2.981	5.58	2.500	4.86	0.097
400	6.88	2.474	7.59	1.850	5.43	0.087

Where, D_1 and C_1 are hydrogen diffusion coefficient and electrolysis hydrogen charging concentration at the weld respectively; D_2 and C_2 are hydrogen diffusion coefficient and electrolysis hydrogen charging concentration at the heat-affected zone respectively; D_3 and C_3 are hydrogen diffusion coefficient and electrolysis hydrogen charging concentration at the base metal respectively.

4.1.2. Test of Diffused Hydrogen Content in Model II

According to the “Determination Method of Diffused Hydrogen in Deposited Metal” [44], the diffused hydrogen content of the deposited metal (the weld metal formed after the filler metal melted) [14] of Model II was measured using a G4 Phoenix DH analyzer following the thermal conductivity method. The diffused hydrogen content for four specimens from Model II were measured and found to be 3.6875, 3.9375, 3.5179, and 3.4643 ppm. Therefore,

an average value of 3.6518 ppm was used to conduct a numerical simulation of the influence of residual stress on hydrogen diffusion.

4.2. Numerical Simulation of the Influence of Residual Stress on Hydrogen Diffusion in Model II

In this study, the primary source of hydrogen during the welding process was the weld metal, and the influence of welding residual stress on hydrogen diffusion was investigated accordingly. Considering that the transient hydrogen content in the welded joint is difficult to experimentally measure and the change in hydrogen concentration at the weld seam during the diffusion process is difficult to predict [13,22,28,45], the influence of the change in hydrogen concentration at the weld seam was ignored for the simulations in this study; the influence of this factor should be considered in subsequent research.

The heterogeneity of the microstructure in the welded joint led to different hydrogen diffusion properties in each area. Because of the heterogeneity in the structure after welding, the hydrogen diffusion distribution of the microstructure heterogeneity was studied for the residual stress in Model II. The hydrogen diffusion coefficients of the weld, heat-affected zone, and base metal considering the welding residual stress could be obtained according to the hydrostatic stress distribution obtained in Section 3.2.2 (Figure 14) and the hydrogen diffusion coefficient under different tensile stresses (Table 4) of various zones in Model II (tested in Section 4.1.1), which were 6.04×10^{-11} , 5.58×10^{-11} , and $4.16 \times 10^{-11} \text{ m}^2/\text{s}$, respectively.

Combined with the weld hydrogen concentration of 3.6518 ppm obtained in Section 4.1.2, the hydrogen concentration distribution in Model II under the influence of the heterogeneous microstructure and residual stress when the model reached a steady state was obtained, as shown in Figure 19. The concentration distribution of hydrogen diffusion along Paths 2 and 3 (Figure 9a) in Model II are shown in Figure 20. Figures 19 and 20 show the following:

1. Perpendicular to the weld (Path 2), the hydrogen concentration after diffusion presented a bimodal distribution with a maximum hydrogen concentration near the weld toe of approximately 6.1 ppm.
2. Along the weld toe (Path 3), the hydrogen concentration changed gently, with a maximum value of approximately 6.22 ppm.

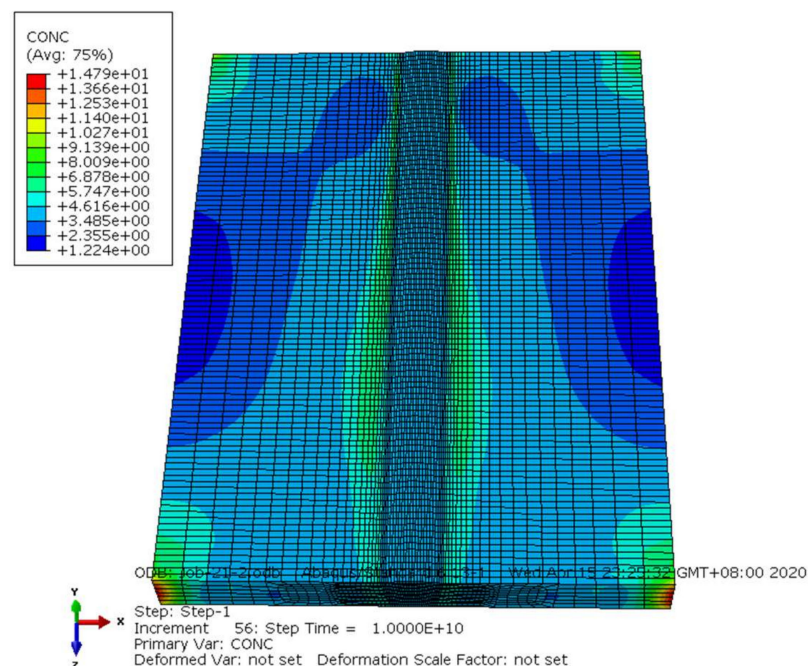


Figure 19. Hydrogen concentration distribution in Model II.

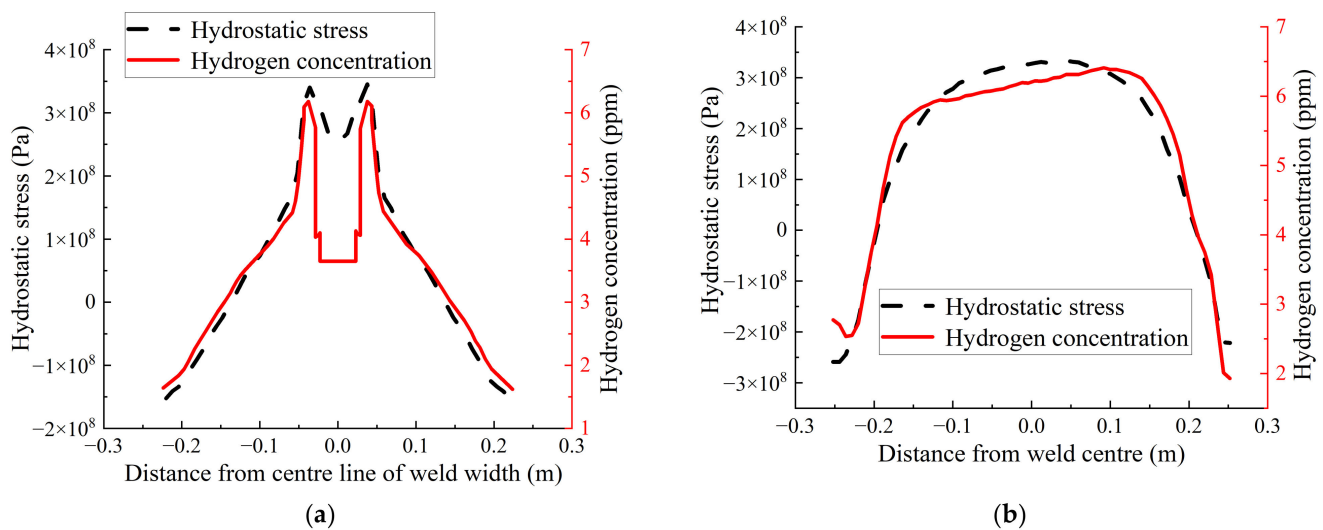


Figure 20. Hydrogen concentration distribution under the influence of hydrostatic stress and heterogeneous microstructure of Model II for (a) Path 2; (b) Path 3.

The hydrostatic stress (Figure 14) and hydrogen concentration distribution considering the welding residual stress along Paths 2 and 3 of Model II are shown in Figure 20, which demonstrate the following:

1. The distribution of hydrogen concentration in the model was consistent with that of hydrostatic stress.
2. Hydrogen diffused to accumulate in regions of larger tensile stress when the influence of the heterogeneous microstructure of the welded joint was considered, that is, the concentration of hydrogen was higher in regions experiencing high welding residual tensile stress.

5. Discussion

Although the effect of welding residual stress on hydrogen diffusion has been studied by combining numerical simulations and experiments, these studies focused on thin shells or thin plates with low yield strength [16,27–29]. In this study, high-thickness (as high-strength steels are sensitive to residual stress [6,46–48]) butt-welded (which causes complex residual stress) high-strength steel plates used for ship structures were studied.

The residual stress of typical butt-welded marine high-strength thick steel plates was studied by three-dimensional numerical simulations, and the hydrogen diffusion coefficient was studied using electrochemical and hydrogen collection methods. The distribution of hydrogen under the influence of residual stress in thick butt-welded high-strength steel plates was obtained from the combination of experimental research and numerical simulations. Phase transformation and hydrogen-induced cracking will be considered in subsequent studies.

6. Conclusions

In this study, the residual stress of thick butt-welded high-strength steel plates was numerically simulated using thermoelastic–plastic theory and the double ellipsoidal heat source model. The feasibility of the numerical simulation method for welding residual stress was obtained by comparing it with the relevant test results in the literature. Next, the hydrogen diffusion coefficients in the weld, heat-affected zone, and base metal regions of the thick butt-welded high-strength steel plates were experimentally obtained. Finally, on the basis of the basic theory of stress-induced hydrogen diffusion and the previously obtained diffusion coefficients, the hydrogen diffusion distribution was numerically simulated under the influence of residual stress. The following conclusions can be drawn from the results of this study:

1. There was a large hydrostatic tensile stress concentration in the weld and heat-affected zone of Model II. The hydrostatic tensile stress in the vertical weld path was maximized (~345 MPa) near the weld toe and presented a symmetrical bimodal distribution.
2. The distribution of hydrogen in Model II was consistent with that of hydrostatic stress, which reached a maximum near the weld toe (the maximum value of Path 2 was approximately 6.1 ppm, and the maximum value of Path 3 was approximately 6.22 ppm). When the hydrostatic stress was tensile, diffusion and accumulation of hydrogen were promoted in the welded joint, so the hydrogen concentration was higher in regions with higher tensile stress.
3. The toe of the butt weld was the weakest area of the entire thick high-strength steel plate model, where both the hydrostatic stress and concentration were high. These conditions will degrade the material properties and cause hydrogen-related cracking.
4. A reliable numerical simulation method combined with laboratory tests for the effect of residual stresses in thick butt-welded high-strength steel plates on hydrogen diffusion was obtained.

Note that owing to difficulties in experimentally measuring the transient hydrogen content in a welded joint and predicting the change in hydrogen concentration at a weld seam during the diffusion process, the influence of the change in hydrogen concentration at the weld seam was ignored in this study. The influence of this factor on hydrogen diffusion due to residual stress should be considered in future research.

Author Contributions: Conceptualization, J.J. and L.L.; methodology, W.Z.; software, W.Z.; funding acquisition, L.L.; validation, J.J.; supervision, L.L.; formal analysis, J.J.; writing—original draft, W.Z. All authors have read and agreed to the published version of the manuscript.

Funding: This work was supported by the National Natural Science Foundation of China (NSFC) (Grant number 5217110689).

Institutional Review Board Statement: Not applicable.

Informed Consent Statement: Not applicable.

Data Availability Statement: All data are included in the manuscript.

Conflicts of Interest: The authors declare no conflict of interest.

References

1. Li, Y.J.; Wu, A.P.; Quan, L.I.; Yue, Z.H.A.O.; Zhu, R.C.; Wang, G.Q. Effects of Welding Parameters on Weld Shape and Residual Stresses in Electron Beam Welded Ti2AlNb Alloy Joints. *Trans. Nonferrous Met. Soc. China* **2019**, *29*, 67–76. [[CrossRef](#)]
2. Xie, P.; Zhao, H.Y.; Wu, B.; Gong, S.L. Using Finite Element and Contour Method to Evaluate Residual Stress in Thick Ti-6Al-4V Alloy Welded by Electron Beam Welding. *J. Acta Metall. Sin.* **2015**, *28*, 922–930. [[CrossRef](#)]
3. Takayama, K.; Matsumoto, R.; Taketomi, S.; Miyazaki, N. Hydrogen Diffusion Analyses of a Cracked Steel Pipe under Internal Pressure. *Int. J. Hydrog. Energy* **2011**, *36*, 1037–1045. [[CrossRef](#)]
4. Rogante, M.; Battistella, P.; Cesari, F. Hydrogen Interaction and Stress-Corrosion in Hydrocarbon Storage Vessel and Pipeline Weldings. *Int. J. Hydrog. Energy* **2006**, *31*, 597–601. [[CrossRef](#)]
5. Niwa, M.; Shikama, T.; Yonezu, A. Mechanism of Hydrogen Embrittlement Cracking Produced by Residual Stress from Indentation Impression. *J. Mater. Sci. Eng. A* **2015**, *624*, 52–61. [[CrossRef](#)]
6. Shi, X.; Yan, W.; Wang, W.; Shan, Y.; Yang, K. Novel Cu-Bearing High-Strength Pipeline Steels with Excellent Resistance to Hydrogen-Induced Cracking. *Mater. Des.* **2016**, *92*, 300–305. [[CrossRef](#)]
7. Cui, C.J.; Peng, Q. Study on Hydrogen Permeation Process in Titanium and Ti Alloys. *Rare Met. Mater. Eng.* **2003**, *12*, 1011–1015.
8. Sant’Anna, A.M.D.S.; Bastos, I.N.; Rebello, J.M.A.; Fonseca, M.P.C. Influence of Hydrogenation on Residual Stresses of Pipeline Steel Welded Joints. *Mater. Res.* **2016**, *19*, 1088–1097. [[CrossRef](#)]
9. Roy, K.; Lau, H.H.; Fang, Z.; Masood, R.; Ting, T.C.; Lim, J.B.; Lee, V.C. *Effects of Corrosion on the Strength of Self-Drilling Screw Connections in Cold-Formed Steel Structures—Experiments and Finite Element Modeling, Structures*; Elsevier: Amsterdam, The Netherlands, 2022; Volume 36, pp. 1080–1096.
10. Feng, R.; Huang, Z.; Chen, Z.; Roy, K.; Chen, B.; Lim, J.B. Experimental study on material properties and stress concentration factors of stainless-steel hybrid tubular joints. *Constr. Build. Mater.* **2021**, *267*, 121103. [[CrossRef](#)]
11. Tomków, J.; Landowski, M.; Fydrych, D.; Rogalski, G. Underwater wet welding of S1300 ultra-high strength steel. *J. Mar. Struct.* **2022**, *81*, 103120. [[CrossRef](#)]

12. Pandey, C.; Mahapatra, M.M.; Kumar, P.; Saini, N. Effect of Weld Consumable Conditioning on the Diffusible Hydrogen and Subsequent Residual Stress and Flexural Strength of Multipass Welded P91 Steels. *J. Metall. Mater. Trans. B* **2018**, *49*, 2881–2895. [[CrossRef](#)]
13. Jiang, W.C.; Gong, J.M.; Tang, J.Q. Numerical Simulation of Hydrogen Diffusion under Welding Residual Stress. *J. Trans. China Weld. Inst.* **2006**, *27*, 57–60.
14. Jiang, W.C.; Gong, J.M.; Tang, J.Q.; Chen, H.; Tu, S. 3-D Finite Element Analysis of the Effect of Welding Residual Stress on Hydrogen Diffusion in Hydrogen Contained Environment. *J. Acta Metall. Sin.* **2007**, *20*, 347–354. [[CrossRef](#)]
15. Jiang, W.C.; Gong, J.M.; Tang, J.Q.; Chen, H. Finite Element Simulation of Influence of Welding Residual Stress on Hydrogen Diffusion. *J. Acta Metall. Sin.* **2006**, *42*, 1221–1226.
16. Lv, L.X.B.; Zheng, B.L.; Xi, Q. Numerical Analysis of Hydrogen Diffusion under Residual Stress of Welding Joints. In Proceedings of the 4th Marine Materials and Corrosion Protection Congress, Prague, Czech Republic, 7 September 2017.
17. Li, L.B.; Jia, Q.Q.; Wan, Z.Q. *Effect of Residual Stress on Hydrogen Diffusion in Flat Butt Welding Joints. Practical Design of Ships and Other Floating Structures*; Springer: Singapore, 2019; Volume 64, pp. 652–665.
18. Zhang, J.; Dai, M.; Wang, F.; Tang, W.; Zhao, X.; Zhu, Y. Theoretical and experimental study of the free hydroforming of egg-shaped shell. *J. Ships Offshore Struct.* **2022**, *17*, 257–267. [[CrossRef](#)]
19. Zhang, J.; Hu, H.; Wang, F.; Li, Y.; Tang, W. Buckling of externally pressurized torispheres with uniform and stepwise thickness. *J. Thin Wall Struct.* **2022**, *173*, 109045. [[CrossRef](#)]
20. Zhang, J.; Liu, C.; Tang, W.; Wang, F.; Zhao, X.; Zhang, J.; Tang, L. Collapse of barreled frustums under external hydrostatic pressure. *J. Mar. Struct.* **2022**, *84*, 103218. [[CrossRef](#)]
21. Zhang, J.; Cheng, P.; Wang, F.; Tang, W.; Zhao, X. Hydroforming and buckling of an egg-shaped shell based on a petal-shaped preform. *J. Ocean. Eng.* **2022**, *250*, 111057. [[CrossRef](#)]
22. Zhang, T.M. Hydrogen-Induced Embrittlement of X80 Steel Welded Joints in High-Pressure Coal Gas Pipeline. Ph.D. Thesis, CUPB, Qingdao, China, 2016.
23. Zhang, T.M.; Wang, Y.; Zhao, W.M.; Wu, Q. Hydrogen Embrittlement Sensitivity of X80 Pipeline Steel and HAZ under Simulated Coal-to-Gas Environment. *J. Trans. China Weld. Inst.* **2015**, *36*, 43–46.
24. Zhang, T.M.; Wang, Y.; Zhao, W.M. Hydrogen Permeability Parameters of X80 Steel and Heat-Affected Zone under High Pressure Coal-Gas Production. *J. Acta Metall. Sin.* **2015**, *51*, 1101–1110.
25. Zhao, W.M.; Zhang, T.M.; Zhao, Y.J.; Sun, J.; Wang, Y. Hydrogen Permeation and Embrittlement Susceptibility of X80 Welded Joint under High-Pressure Coal Gas Environment. *J. Corros. Sci.* **2016**, *111*, 84–97. [[CrossRef](#)]
26. Gong, J.M.; Jiang, W.C.; Tang, J.Q.; Tu, S.D. Numerical Simulation of Hydrogen Diffusion in Welded Joint of Low Alloy Steel in Wet H₂S Environment. *J. Trans. China Weld. Inst.* **2007**, *28*, 5–8.
27. Yan, C.Y.; Liu, C.Y.; Yan, B. 3D Modeling of the Hydrogen Distribution in X80 Pipeline Steel Welded Joints. *J. Comp. Mater. Sci.* **2014**, *83*, 158–163. [[CrossRef](#)]
28. Yan, C.Y.; Zhang, G.Y.; Liu, G.Y. Numerical Simulation of Hydrogen Distribution in X80 Pipeline Steel Welded Joints. *J. Trans. China Weld. Inst.* **2015**, *36*, 103–107.
29. Yan, C.Y.; Liu, G.Y.; Zhang, G.Y. Simulation of Hydrogen Diffusion in Welded Joint of X80 Pipeline Steel. *J. Cent. South Univ.* **2014**, *21*, 4432–4437. [[CrossRef](#)]
30. Chen, G. Study on the Influence of Residual Stress on Fatigue Crack Propagation of Typical Welded Joints. Master's Thesis, Jiangsu University of Science and Technology, Zhenjiang, China, 2019.
31. Hua, Y.P. Numerical Simulation of T-Welding Residual Stress and Strength Analysis. Master's Thesis, Dalian University of Technology, Dalian, China, 2009.
32. Zhang, T.M.; Zhao, W.M.; Jiang, W. Numerical Simulation of Hydrogen Diffusion in X80 Welded Joint under the Combined Effect of Residual Stress and Microstructure Inhomogeneity. *J. Acta Metall. Sin.* **2019**, *55*, 258–266.
33. Liu, C.; Luo, Y.; Yang, M.; Fu, Q. Effects of material hardening model and lumped-pass method on welding residual stress simulation of j-groove weld in nuclear RPV. *Eng. Comput.* **2016**, *33*, 1435–1450. [[CrossRef](#)]
34. Liu, C.; Luo, Y.; Yang, M.; Fu, Q. Three-dimensional finite element simulation of welding residual stress in RPV with Two J-groove Welds. *Weld. World* **2017**, *61*, 151–160. [[CrossRef](#)]
35. Sun, W.T. Numerical Prediction and Comparative Experimental Study on Welding Residual Stress of Submarine General Section Closure. Master's Thesis, China Shipbuilding Research Center, Wuxi, China, 2006.
36. Goldak, J.; Chakravarti, A.; Bibby, M. A New Finite Element Model for Welding Heat Sources. *Metall. Trans. B* **1984**, *15*, 299–305. [[CrossRef](#)]
37. Liu, Y. Study on Mechanical Behavior of Welding Repair Welding of High Strength Steel Considering Solid State Phase Transformation Effect. Master's Thesis, Harbin Institute of Technology, Harbin, China, 2016.
38. Li, R.Y.; Zhao, M.; Wu, C.M. Determination of Shape Parameters of Double Ellipsoid Heat Source Model in Numerical Simulation Based on SYSWELD Software. *J. Trans. China Weld. Inst.* **2014**, *35*, 93–96.
39. Ouyang, Y.J. Study on Hydrogen Diffusion and Hydrogen Penetration Sensor in Steel. Ph.D. Thesis, Hunan University, Changsha, China, 2013.
40. Wang, Z. Study on Hydrogen Diffusion and Its Effect on Hydrogen Embrittlement of High Strength DP Steels. Ph.D. Thesis, Wuhan University of Science and Technology, Wuhan, China, 2021.

41. Devanathan, M.A.V.; Stachurski, Z. The Adsorption and Diffusion of Electrolytic Hydrogen in Palladium. *J. Proc. R. Soc. Lond. Ser. A Math. Phys. Sci.* **1962**, *270*, 90–102.
42. Li, J.; Du, F.S.; Liang, Y.; Wu, S.; Tan, T. Hydrogen diffusion calculation experiment of sheet metal. *J. Steel* **2016**, *51*, 70–75.
43. Fu, L. Failure Criterion for Hydrogen Induced Cracking Based on Fracture Mechanics Theory and Molecular Dynamics Simulation. Harbin. Ph.D. Thesis, Institute of Technology, Harbin, China, 2019.
44. Jiang, Y.L.; Yang, Z.J.; Song, B.; Sun, X.M.; Yuan, H.; Jia, M. Current status and analysis of standard methods for determination of diffused hydrogen in deposited metals. *J. Jixie Zhizao Wenzhai* **2020**, *2020*, 20–26.
45. Zhang, X.H.; Tan, C.Y.; Chen, P.Y. Numerical Simulation of Hydrogen Diffusion in Welded Joints (I). *J. Trans. China Weld. Inst.* **2000**, *21*, 51–54.
46. Taljat, B.; Radhakrishnan, B.; Zacharia, T. Numerical Analysis of GTA Welding Process with Emphasis on Post-Solidification Phase Transformation Effects on Residual Stresses. *J. Mater. Sci. Eng. A* **1998**, *246*, 45–54. [[CrossRef](#)]
47. Fratini, L.; Pasta, S.; Reynolds, A.P. Fatigue Crack Growth in 2024-T351 Friction Stir Welded Joints: Longitudinal Residual Stress and Microstructural Effects. *Int. J. Fatigue* **2009**, *31*, 495–500. [[CrossRef](#)]
48. Fratini, L.; Zuccarello, B. An Analysis of through-Thickness Residual Stresses in Aluminium FSW Butt Joints. *Int. J. Mach. Tools Manuf.* **2006**, *46*, 611–619. [[CrossRef](#)]